



# Quantification of the Writhe Number of the Evolution of Solar Filament Axes

Zhenjun Zhou (周振军)<sup>1,2,3,4</sup> , Chaowei Jiang<sup>5</sup> , Hongqiang Song<sup>6</sup> , Yuming Wang<sup>3</sup> , Yongqiang Hao<sup>1</sup> , and Jun Cui<sup>1</sup> 

<sup>1</sup> Planetary Environmental and Astrobiological Research Laboratory (PEARL), School of Atmospheric Sciences, Sun Yat-sen University, Zhuhai, People's Republic of China; [zhouzhj7@mail.sysu.edu.cn](mailto:zhouzhj7@mail.sysu.edu.cn)

<sup>2</sup> Key Laboratory of Tropical Atmosphere-Ocean System, Sun Yat-sen University, Ministry of Education, Zhuhai, People's Republic of China

<sup>3</sup> CAS Key Laboratory of Geospace Environment, University of Science and Technology of China, Hefei, Anhui 230026, People's Republic of China

<sup>4</sup> CAS Center for Excellence in Comparative Planetology, Hefei, People's Republic of China

<sup>5</sup> Institute of Space Science and Applied Technology, Harbin Institute of Technology, Shenzhen 518055, People's Republic of China

<sup>6</sup> Shandong Provincial Key Laboratory of Optical Astronomy and Solar-Terrestrial Environment, and Institute of Space Sciences, Shandong University, Weihai, Shandong 264209, People's Republic of China

Received 2022 September 9; revised 2023 January 24; accepted 2023 January 27; published 2023 February 22

## Abstract

Solar filament eruptions often show complex and dramatic geometric deformation that is highly relevant to the underlying physical mechanism triggering the eruptions. It is well known that the writhe of filament axes is a key parameter characterizing its global geometric deformation, but a quantitative investigation of the development of writhe during its eruption is still lacking. Here we introduce the Writhe Application Toolkit, which can be used to characterize accurately the topology of filament axes. This characterization is achieved based on the reconstruction and writhe number computation of three-dimensional paths of the filament axes from dual-perspective observations. We apply this toolkit to four dextral filaments located in the northern hemisphere with a counterclockwise (CCW) rotation during their eruptions. Initially, all these filaments possess a small writhe number ( $\leq 0.20$ ) indicating a weak helical deformation of the axes. As the CCW rotation kicks in, their writhe numbers begin to decrease and reach large negative values. Combined with the extended Călugăreanu theorem, the absolute value of twist is deduced to decrease during the rotation. Such a quantitative analysis strongly indicates a consequence of the conversion of twist into writhe for the studied events.

*Unified Astronomy Thesaurus concepts:* [Solar filament eruptions \(1981\)](#); [Solar filaments \(1495\)](#); [Solar prominences \(1519\)](#)

*Supporting material:* animation

## 1. Introduction

Solar magnetic flux ropes (MFRs), defined as a group of twisted magnetic field lines wrapped around a common axis, are core structures driving solar eruptions such as flares and coronal mass ejections. The writhe of the MFR's axis is a fundamental parameter for characterizing its global geometric deformation, which has been found to be highly correlated with the dynamic property of MFRs. Many observational features in the corona reveal MFRs with writhed axes from different observational wavelengths and perspectives. For example, the presence of S-shaped structures on the solar disk, like sigmoids observed in the extreme ultraviolet (EUV) and soft X-ray passbands, are expected to be the manifestation of enhanced current density in MFRs (Kliem et al. 2004; Gibson et al. 2006). The filament, often observed underneath a cospatial sigmoid, is embedded in the bottom of the MFR (Cheng et al. 2014). Thus, the shape of a filament is an alternative substitution to trace the MFR's axis (Zhou et al. 2017).

Besides a distorted axis, filament often exhibits an internal twisted structure. By tracing the threads of filament about its axis in high-resolution observations, like the Swedish 1 m Solar Telescope (Scharmer et al. 2003) and the New Vacuum Solar Telescope (Liu et al. 2014), spiral structures and motions are frequently observed (e.g., Schmieder et al. 2000). The bright

and dark signals as observed on opposite sides of a filament in both the  $H\alpha$  and its corresponding line-of-sight velocity (Doppler) observations suggest that interwinding threads follow the helical field lines inside filament. These observational facts exhibit helical threads wrapping around the axis, in favor of the existence of considerable twist, and an overall distorted shape, indicating a writhed axis.

When erupted, the spinning motions observed in jets, as well as apex rotations in erupting filaments, suggest a relaxation of magnetic twist, thus lowering the magnetic energy of the MFR by reducing the bending of its field lines. In particular, under the ideal MHD constraint of helicity conservation, the rotation of the filament axis in the course of its rise is generally interpreted as a consequence of the conversion of twist into writhe. Numerical simulations (Kliem et al. 2012; Hassanin & Kliem 2016) recreate this rotation motion in a kink-unstable MFR. Kink instability serves as the key mechanism leading to the rotation. It refers to the helical instability of the MFR that commences when the twist of the rope exceeds some critical value (Török et al. 2004). This instability has received great attention due to its good quantitative agreement with many well-observed events (Török & Kliem 2005; Williams et al. 2005; Kliem et al. 2012). Another rotation mechanism, the Lorentz force due to the external sheared field, is also addressed as a major contributor to driving the filament rotating (Isenberg & Forbes 2007; Kliem et al. 2012).

Observations show that clockwise (CW)/counterclockwise (CCW) rotation is associated with sinistral/dextral filaments (Green et al. 2007; Zhou et al. 2020), no matter whether the rotation is triggered by the kink instability or the external

sheared field (Isenberg & Forbes 2007; Kliem et al. 2012). However, this leaves a mystery (Zhou et al. 2022): sinistral/dextral filaments often exhibit a forward/reverse S shape, while through a CW/CCW rotation, the filament spine is straightened and even over-rotated to reverse its initial shape. During this process, the writhe number of the spine seems to experience a decreasing process, though such a variation has never been systematically investigated.

Revealing the variation of the writhe number for a filament axis during its rotation is a key step in understanding which mechanism triggers the eruptions. However, this temporal evolution has hardly been quantified, even for numerical simulations that provide the three-dimensional (3D) magnetic field of erupting, kinked flux ropes (Linton et al. 1998). The general definition of writhe number makes its computation a relatively complicated task. Moreover, in reality, it is difficult to obtain the 3D geometry of a filament axis to limited observations.

In this paper, we report the development of the Writhe Application Toolkit (WAT) for computing precisely the writhe number of solar filaments and its application to quantitative investigation of writhe number variation in four filament eruptions. These eruptions are recorded from dual-perspective observations with the dramatic development of writhe during rotations. In the sections that follow, an introduction to the instruments and methods is presented in Section 2. A detailed analysis of a typical example is given in Section 3. And finally, we summarize and discuss our results in Sections 4 and 5.

## 2. Observation and Analysis

### 2.1. Instruments and Methods

Our computation is based on the dual-perspective observations from two spacecraft. The Solar TERrestrial Relations Observatory (STEREO; Kaiser et al. 2008) mission consists of two spacecraft placed in heliocentric orbits ahead of (STEREO-A) and behind (STEREO-B) Earth. As viewed from the Sun, these two spacecraft moved away from Earth at approximately  $22^\circ$  per year in opposite directions. Meanwhile, the Solar Dynamics Observatory (SDO; Pesnell et al. 2012) was placed in the geosynchronous orbit. The paired Extreme Ultraviolet Imager (EUVI; Wuelser et al. 2004) telescopes on board STEREO can observe a filament in narrow EUV passbands including  $195 \text{ \AA}$  (formation temperature,  $T_f \simeq 1.6 \times 10^6 \text{ K}$ ) and  $304 \text{ \AA}$  ( $\simeq 6 \sim 8 \times 10^5 \text{ K}$ ). The typical cadences for these two filters are 5 and 10 minutes. The Atmospheric Imaging Assembly (AIA; Lemen et al. 2012) on board SDO has similar filters of  $193 \text{ \AA}$  ( $\simeq 1.58 \times 10^6 \text{ K}$ ) and  $304 \text{ \AA}$  ( $\simeq 10^5 \text{ K}$ ) channels with a higher cadence (12 s). Their simultaneous observations in a multi-view setting allow us to perform stereoscopic triangulation on a solar filament. Meanwhile, the Helioseismic and Magnetic Imager (HMI; Hoeksema et al. 2014) on board SDO provides the vector magnetograms which is conducive to the determination of filament chirality.

To get the 3D configuration of a filament, we employ the `scc_measure` widget application (Thompson 2009) in the Solar SoftWare library, which uses a tie-pointing method for reconstruction (Inhester 2006). We first select a point along the filament spine in, for example, the AIA image, then this routine will calculate a path representing the line of sight from another perspective displayed in, for example, the EUVI image. According to the dynamic evolution and emission

characteristics, the same feature point along this path can be identified manually. Its 3D coordinates (heliographic longitude, latitude, and radial distance in solar radii) are then calculated. The steps above are repeated until the entire filament axis, including its footpoints, is reconstructed.

The positional data of the filament axis are then smoothed and interpolated using 3D cubic B-splines, with the aid of the SciPy `interpolate.splprep` module and the smoothing factor is set to 0.0005. The position of the spline is evaluated using the `interpolate.splev` module.

The reconstruction, smoothing, and interpolating of the filament axis at all time frames follow the same processing procedures. Thus, during the eruption, the evolution of the filament axis, including the rotation and expanding motion, can be studied in three dimensions.

A new definition of writhe, termed the polar writhe  $\mathcal{W}_p$  (Berger & Prior 2006), is designed to measure the writhe of open curves with endpoints on a boundary plane. This definition is especially appropriate to quantify the helical deformation of the filament axis. The computation of the polar writhe  $\mathcal{W}_p$  is decomposed into local and nonlocal components:

$$\mathcal{W}_p(\mathbf{r}) = \mathcal{W}_{pl}(\mathbf{r}) + \mathcal{W}_{pnl}(\mathbf{r}), \quad (1)$$

Here the curve is divided into  $n + 1$  pieces at  $n$  turning points ( $ds/dz = 0$ ) in vertical direction  $z$ . The local writhe ( $\mathcal{W}_{pl}$ ) measures helical coiling in each individual piece, where the nonlocal polar writhe ( $\mathcal{W}_{pnl}$ ) gives a quantitative calculation of the global geometric relations between these pieces.  $\mathcal{W}_{pl}$  and  $\mathcal{W}_{pnl}$  can be calculated as (Berger & Prior 2006):

$$\mathcal{W}_{pl} = \sum_{i=1}^{n+1} \frac{1}{2\pi} \int_{z_i^{\min}}^{z_i^{\max}} \frac{\mathbf{z} \cdot \mathbf{T}_i \times \frac{d\mathbf{T}_i}{dz} dz}{1 + |\mathbf{z} \cdot \mathbf{T}_i|}, \quad (2)$$

$$\mathcal{W}_{pnl} = \sum_{i=1}^{n+1} \sum_{\substack{j=1 \\ i \neq j}}^{n+1} \frac{\sigma_{ij}}{2\pi} \int_{z_{ij}^{\min}}^{z_{ij}^{\max}} \frac{d\Theta_{ij}}{dz} dz, \quad (3)$$

where  $i, j$  are two different pieces,  $\mathbf{T}_i = d\mathbf{x}_i/ds$  is the unit tangent vector of the piece  $\mathbf{x}_i$ , the indicator function  $\sigma_{ij} = +1$  if these two pieces are moving toward the same direction, and  $\sigma_{ij} = -1$  if two pieces are moving in opposite directions.  $\Theta_{ij}$  is the orientation of the relative position vector ( $\mathbf{r}_{ij} = \mathbf{x}_j - \mathbf{x}_i$ ) with respect to the  $x$ -axis. Based on Equations (1)–(3), a tool for the numerical computation of the polar writhe is available online (Prior & Neukirch 2016).<sup>7</sup> We applied this code to the calculation of the writhe for the filament axis.

All these processes above are integrated into a publicly available package called the Writhe Application Toolkit<sup>8</sup> (WAT).

### 2.2. Selection of Events

Through browsing image data for solar filament eruption in the past 12 yr since the launch of SDO, four cases are chosen following the criteria below: (1) An obvious rotation motion can be observed during the filament eruption. (2) The entire filament, including its footpoints, is required to be observed from at least two different perspectives. The SDO/AIA observation from the perspective of Earth is a necessity as its

<sup>7</sup> <https://www.maths.dur.ac.uk/~ktch24/code.html>

<sup>8</sup> <http://sysu-pearl.cn:8080/writhecode>

**Table 1**  
Properties of the Selected Filaments

No.	Start Time	Observations			Inferred Properties			References <sup>a</sup>
		Hemisphere	Projection Shape	Rotation	Chirality	Initial Writhe	Trend	
1	2010-12-10 06:06	N	Z	CCW	Dextral	0.107	Decrease	<a href="#">S18</a>
2	2011-12-25 07:50	N	Z	CCW	Dextral	0.206	Decrease	<a href="#">Z20</a>
3	2012-05-05 17:15	N	Z	CCW	Dextral	-0.024	Decrease	<a href="#">Z19,Z20</a>
4	2012-10-25 03:36	N	S	CCW	Dextral	0.075	Decrease	<a href="#">Z19,Z20</a>

**Note.**

<sup>a</sup> Previous investigations of the filament eruption. [S18](#) refers to Song et al. (2018), [Z19](#) to Zhou et al. (2019), and [Z20](#) to Zhou et al. (2020).

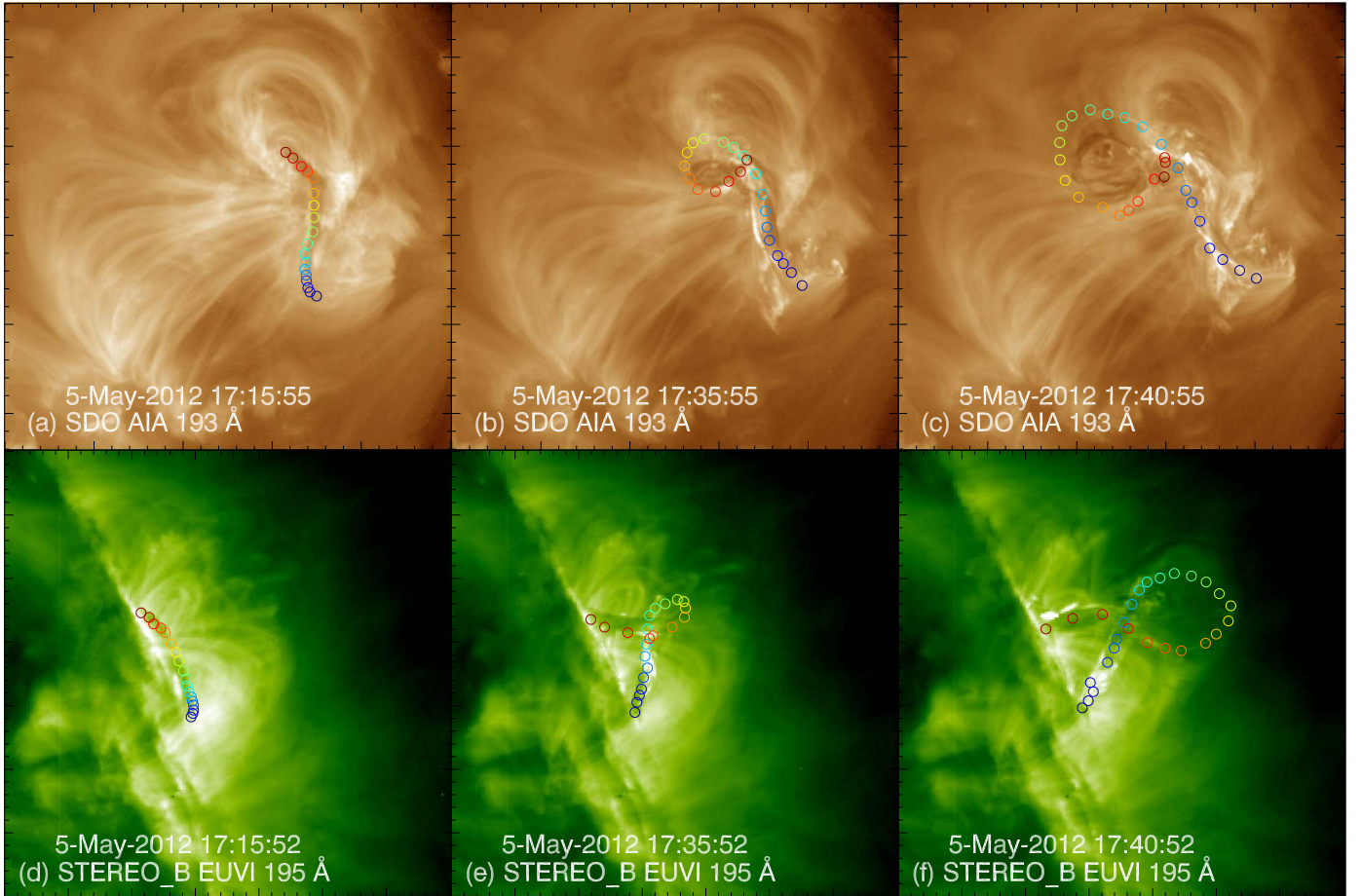


**Figure 1.** Filament rotation during its eruption on 2012 May 5. (a)–(c) AIA 193 Å images at 17:15, 17:35, and 17:40 UT displaying the top view of the evolution of this filament rotation. (d)–(f) The EUVI B 195 Å images showing the side view of the filament rotation. The color-coded points mark identical points on the Sun as seen from STEREO-B and SDO, respectively. An animation of AIA 193 Å and EUVI 195 Å direct images is available online to show the rotation of the filament. The video covers the time from 17:15:07–17:50:55 UT with a cadence of 12 s, and its duration is 9 s.

(An animation of this figure is available.)

high cadence ensures simultaneously imaging the Sun with STEREO. The selected filament eruptions and their properties are listed in Table 1, including the direct observational characteristics and inferred properties. Details of the selected events (including the dual-perspective imaging observations and the reconstructed position of the filament axes) are available at this [catalog website](#).<sup>9</sup>

### 3. Calculation of the Evolution of Writhe

Among the four cases in Table 1, we take Case #3 as an example (see Figure 1). This filament has dextral chirality as inferred from its left-skewed drainage sites (Figure 2(a)) (Chen et al. 2014; Zhou et al. 2020). The filament eruption occurred on 2012 May 5 at 17:15 UT. It is observed in NOAA Active Region (AR) 11474 at N16E35 from SDO’s view. It is also captured by STEREO-B from the limb view. At that time, the separation angle between SDO and STEREO-B is 118°. In the SDO AIA 193 Å channel (Figure 1(a)), the initial shape of the filament takes on a reverse S shape. When erupting, the

<sup>9</sup> <http://sysu-pearl.cn:8080/solarEruptive>



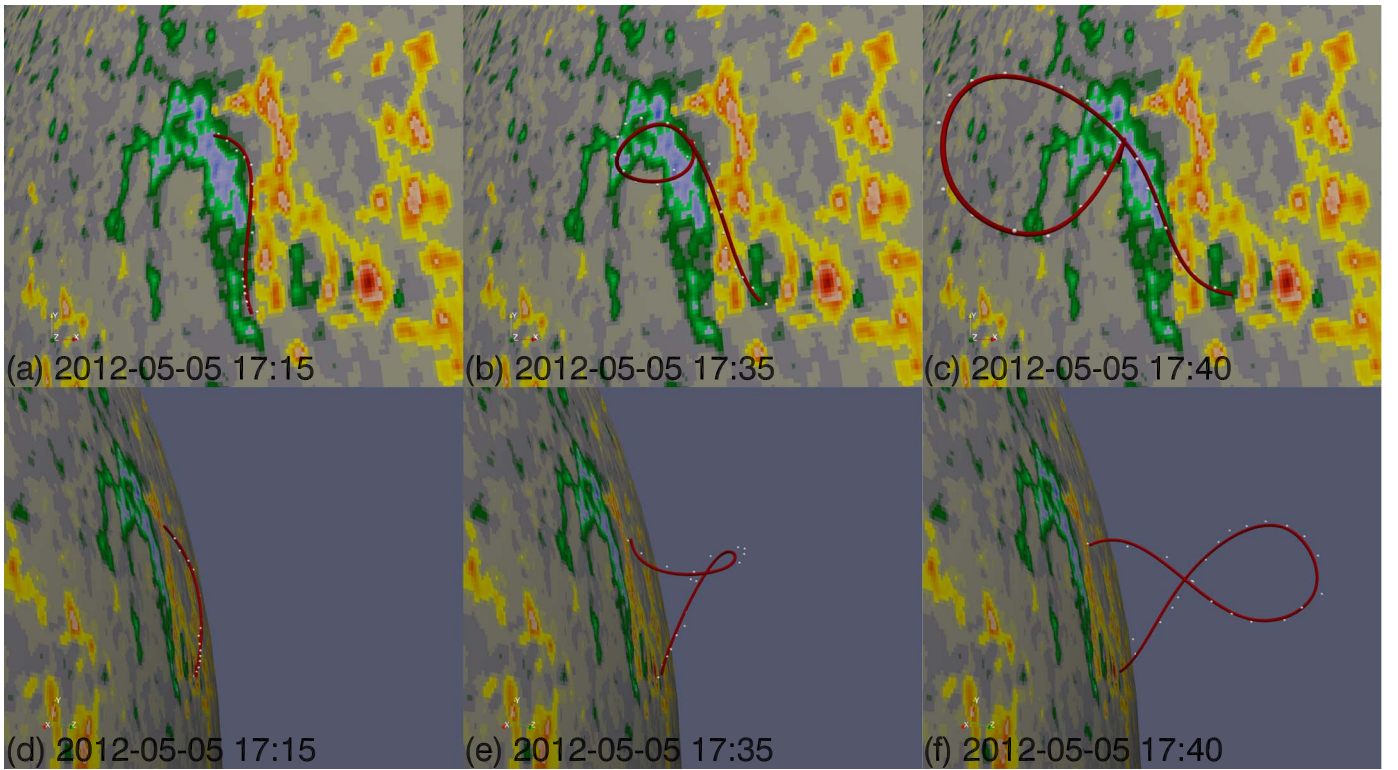


**Figure 2.** The 3D reconstruction of the filament axis during the eruption viewed from the top (a)–(c) and side (d)–(f). White solid points are measured by triangulation from dual viewing angles, the red solid curves are smoothed and interpolated from white points, and the bottom boundaries are the projected HMI daily update radial synoptic map.

filament shows an obvious CCW rotation about the rising direction (Figure 1(a)–(c)), transforming the morphology of filament from a  $\lambda$  shape to a reversed Y shape as seen in the side view (STEREO-B 195 Å, Figure 1(d)–(f)).

The axis of the filament is identified from SDO and STEREO-B images for each snapshot (the color-coded points in Figure 1). Then the 3D positional information of the axis can be determined by the triangulation. Applying the 3D cubic B splines mentioned above, a smoothed and interpolated filament axis is obtained. Repeating the procedure frame by frame, the evolution of the filament axis during eruption can then be acquired, as illustrated by the red spine in Figure 2.

For each time frame, the writhe of the axis curve is computed using the Prior & Neukirch code. We applied the same processing procedures to the other three cases in Table 1, and the writhe evolutions of these filament axes during the rotation are demonstrated in Figure 3. It should be noted that Cases #2 and #3 are reconstructed with AIA 193 Å and EUVI\_B 195 Å images since they have a higher effective cadence of 5 minutes. Limited by the indistinctness in the 195 or 193 Å images, the reconstruction of filaments for Cases #1 and #4 requires examining the 304 Å images (10 minutes cadence). We repeat the reconstruction 5 times for each case to reduce and estimate the errors introduced by measurement.

#### 4. Results

The variations of writhe and their errors during eruptions are displayed in Figure 3. Initially, all these filaments possess a small writhe number ( $\leq 0.20$ ) indicating a weak helical deformation of the axis. And the writhe trajectory is relatively shallow, the filament is slowly evolving without a large change in geometry. The very steep drop in writhe shown in Figure 3

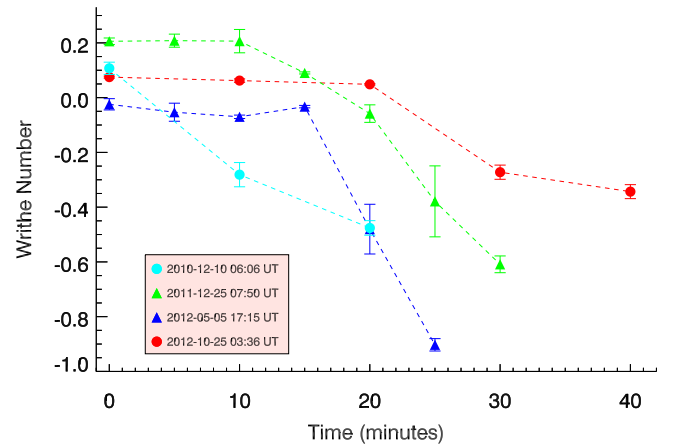


**Figure 3.** The variation of writhe number for filament axes during their eruption. Each event is marked by a different color. Events labeled with triangle symbols are reconstructed from EUVI 195 Å and AIA 193 Å images and with circle symbols reconstructed from EUVI and AIA 304 Å images. The error of the writhe number (marked by the vertical error bar) mainly comes from the uncertainty of feature points' location, which is taken as the standard deviation of 5.

for each case means a strong kinking for the filament geometry; this can be verified in Figure 4: the filaments in the middle subfigures are experiencing transformation into an inverse- $\gamma$  shape from the side view. When the filaments have sufficiently risen, the nonlocal writhe dominates. Actually, this nonlocal writhe measures the apex rotation angle (a nonlocal writhe of  $\pm 2$  indicates one full turn of  $\pm 360^\circ$  for a filament apex rotation) (Török et al. 2010). Meanwhile, Figure 3 shows an interesting fact, which is that the evolution of the writhe shown

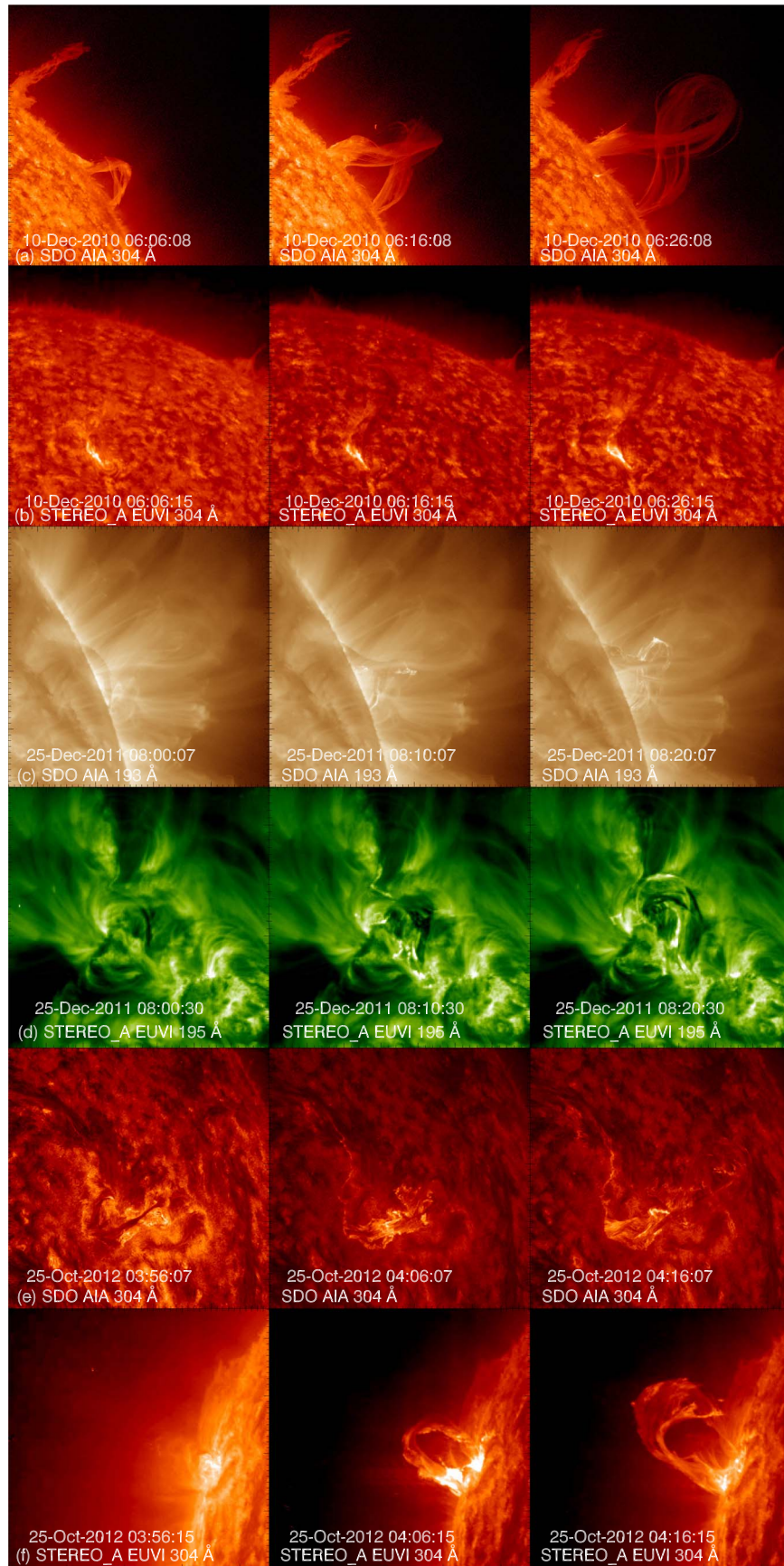


**Figure 4.** Filament rotation during its eruption for the other three cases from dual-perspective observations. Panels (a) and (b) correspond to the cyan dashed line in Figure 3, panels (c) and (d) correspond to the green dashed line, and panels (e) and (f) correspond to the red dashed line.



in the triangle plots (Cases #2 and #3) are very similar to each other but different from the circle ones (Cases #1 and #4). We consider that this results from sample selection bias for the cadence of EUVI 304 Å is 10 minutes and that of EUVI 195 Å is 5 minutes. This implies, to get at least three frames, the rotation we selected in EUVI 304 Å must last for at least 20 minutes, but for cases selected in EUVI 195 Å, the duration can be just 10 minutes. Therefore, the evolution of the writhes selected in EUVI 195 Å (Cases #2 and #3) seems steeper than those in EUVI 304 Å (Cases #1 and #4). Noting that these four cases are located in the northern hemisphere, and due to the mirror symmetry for observational properties between the northern and southern hemispheres, the initial shape and the sense of rotation exhibit opposite behaviors in the southern hemisphere (Zhou et al. 2020). Thus, in the southern hemisphere the writhe should increase during filament rotation.

## 5. Discussion

In this work, we provide a set of processes to reconstruct, smooth, and interpolate the axis of a filament. After that, aided by the Prior & Neukirch code, the writhe of the axis curve is computed. This suite of processes is assembled as the WAT. We apply this toolkit to deal with four filament eruption cases with an obvious rotation motion, and the evolution of the writhe number for solar filament axes is achieved.

These four cases are identified as dextral filaments (Song et al. 2018; Zhou et al. 2019, 2020), implying a negative magnetic helicity being contained (Chae 2000). Helicity can be decomposed into writhe and twist contributions (Berger & Field 1984), thus for a negative helicity field with little or positive writhe ( $\mathcal{W}_p$ ), the sign of the twist ( $\mathcal{T}_w$ ) must be negative. Berger & Prior (2006) extend Călugăreanu theorem to general open curves that are anchored on a plane, like magnetic flux tubes in the solar corona: the net winding ( $\mathcal{L}_p = \mathcal{W}_p + \mathcal{T}_w$ ) is invariant to all motions (as long as the two curves do not intersect and a single curve does not reconnect), so a decrease in writhe must be compensated by an increase in twist (Berger 1984; Linton et al. 1998).

Combining the evolution of writhe in the filament axis, the evolution of the twist for the events studied can be divided into three stages as follows: (1) Initially, the twist number is negative, indicating that the magnetic field lines are left-hand wrapping around the filament axis; (2) As a CCW rotation kicks in,  $\mathcal{W}_p$  decreases to 0. Based on the extended Călugăreanu theorem, there is a corresponding increase in  $\mathcal{T}_w$ . Considering the negative sign, the absolute value of  $\mathcal{T}_w$  should decrease during the rotation. (3) As the CCW rotation continues,  $\mathcal{W}_p$  decreases from 0 to a large negative value, and the trend in the variation in  $\mathcal{T}_w$  is consistent with that in stage 2. It is worth noting that the potential input through or at the photosphere is not considered, due to the small rotation ( $\leq 25^\circ$ , corresponding to 0.069 changes in the net winding  $\mathcal{L}_p$  for sample Case #3) derived from the filament footpoints shifting. Also, the rotation of the filament around the footpoints at the photosphere is too small to identify.

This quantitative analysis of MFR's  $\mathcal{W}_p$  and  $\mathcal{T}_w$  provides an alternative answer to a long-lasting mystery: generally, sinistral/dextral filaments (located in the southern/northern hemisphere) exhibit a forward/reverse S shape, and when erupted, they often rotate CW/CCW when viewed from above, and thus the overall shape of the filaments seem to be straightened or even reversed. In our analysis, the process of

being straightened for a reverse S shape filament corresponds to the decrease of an initially positive writhe to 0. This process is not against the conversion of twist into writhe in the course of flux rope instabilities. The absolute value of  $\mathcal{T}_w$  constantly decreases during the rotation.

In these four cases, the writhe and projected S shape is not unique, and the configurations of the filament axes, including the skewness of filament legs, the filament middle section distorted by the polarity inversion line, the relative height, the position of the highest point, and the position of the crossing point, all contribute to the writhe number (Török et al. 2010; Xu et al. 2020; Zhou et al. 2020). In summary, four filament eruptions in the northern hemisphere with obvious rotation motion are studied in the dual-perspective observations from STEREO and SDO. The evolution of filament axes is obtained with the help of 3D reconstruction and 3D cubic B splines. The polar writhe ( $\mathcal{W}_p$ ) is employed to quantitate the contortion of the filament axis during the rotation. During the eruption,  $\mathcal{W}_p$  decreases from a small value (positive or near 0) to a large negative value. Correspondingly, based on the extended Călugăreanu theorem, the twist ( $\mathcal{T}_w$ ) of a dextral filament (negative helicity contained) should increase. Considering the negative sign of twist, its absolute value decreases during the rotation. This is consistent with the transformation of twist into writhe in a kink-unstable MFR.


The authors appreciate the discussions with Rui Liu, Xin Cheng, and Quanhao Zhang. We acknowledge the SECCHI, AIA, and HMI consortia for providing excellent observations.

This work is supported by the B-type Strategic Priority Program XDB41000000 funded by the Chinese Academy of Sciences. The authors also acknowledge support from the National Natural Science Foundation of China (NSFC 42004142,42274203), Open Research Program of CAS Key Laboratory of Geospace Environment, Science and Technology Project 202102021019 in Guangzhou, the Fundamental Research Funds for the Central Universities (grant No. HIT.BRETIV.201901), and Shenzhen Technology Project JCYJ20190806142609035.

## ORCID iDs

Zhenjun Zhou

(周振军)  <https://orcid.org/0000-0001-7276-3208>

Chaowei Jiang  <https://orcid.org/0000-0002-7018-6862>

Hongqiang Song  <https://orcid.org/0000-0001-5705-661X>

Yuming Wang  <https://orcid.org/0000-0002-8887-3919>

Yongqiang Hao  <https://orcid.org/0000-0002-0073-7198>

Jun Cui  <https://orcid.org/0000-0002-4721-8184>

## References

- Berger, M. A. 1984, *GAJFD*, 30, 79  
 Berger, M. A., & Field, G. B. 1984, *JFM*, 147, 133  
 Berger, M. A., & Prior, C. 2006, *JPhA*, 39, 8321  
 Chae, J. 2000, *ApJL*, 540, L115  
 Chen, P. F., Harra, L. K., & Fang, C. 2014, *ApJ*, 784, 50  
 Cheng, X., Ding, M. D., Zhang, J., et al. 2014, *ApJL*, 789, L35  
 Gibson, S. E., Foster, D., Burkepile, J., de Toma, G., & Stanger, A. 2006, *ApJ*, 641, 590  
 Green, L. M., Kliem, B., Török, T., van Driel-Gesztelyi, L., & Attrill, G. D. R. 2007, *SoPh*, 246, 365  
 Hassanin, A., & Kliem, B. 2016, *ApJ*, 832, 106  
 Inhester, B. 2006, arXiv:astro-ph/0612649  
 Hoeksema, J. T., Liu, Y., Hayashi, K., et al. 2014, *SoPh*, 289, 3483  
 Isenberg, P. A., & Forbes, T. G. 2007, *ApJ*, 670, 1453

- Kaiser, M. L., Kucera, T. A., Davila, J. M., et al. 2008, *SSRv*, 136, 5
- Kliem, B., Titov, V. S., & Török, T. 2004, *A&A*, 413, L23
- Kliem, B., Török, T., & Thompson, W. T. 2012, *SoPh*, 281, 137
- Lemen, J. R., Title, A. M., Akin, D. J., et al. 2012, *SoPh*, 275, 17
- Linton, M. G., Dahlburg, R. B., Fisher, G. H., & Longcope, D. W. 1998, *ApJ*, 507, 404
- Liu, Z., Xu, J., Gu, B.-Z., et al. 2014, *RAA*, 14, 705
- Pesnell, W. D., Thompson, B. J., & Chamberlin, P. C. 2012, *SoPh*, 275, 3
- Prior, C. B., & Neukirch, S. 2016, *JPhA*, 49, 215201
- Scharmer, G. B., Bjelksjö, K., Korhonen, T. K., et al. 2003, *Proc. SPIE*, 4853, 341
- Schmieder, B., Delannée, C., Yong, D. Y., et al. 2000, *A&A*, 358, 728
- Song, H. Q., Zhou, Z. J., Li, L. P., et al. 2018, *ApJL*, 864, L37
- Thompson, W. T. 2009, *Icar*, 200, 351
- Török, T., Berger, M. A., & Kliem, B. 2010, *A&A*, 516, A49
- Török, T., & Kliem, B. 2005, *ApJL*, 630, L97
- Török, T., Kliem, B., & Titov, V. S. 2004, *A&A*, 413, L27
- Williams, D. R., Török, T., Démoulin, P., van Driel-Gesztelyi, L., & Kliem, B. 2005, *ApJL*, 628, L163
- Wuelser, J.-P., Lemen, J. R., Tarbell, T. D., et al. 2004, *Proc. SPIE*, 5171, 111
- Xu, Y., Zhu, J., & Guo, Y. 2020, *ApJ*, 892, 54
- Zhou, Z., Cheng, X., Zhang, J., et al. 2019, *ApJL*, 877, L28
- Zhou, Z., Jiang, C., Liu, R., et al. 2022, *ApJL*, 927, L14
- Zhou, Z., Liu, R., Cheng, X., et al. 2020, *ApJ*, 891, 180
- Zhou, Z., Zhang, J., Wang, Y., Liu, R., & Chintzoglou, G. 2017, *ApJ*, 851, 133